JACS
JOURNAL OF THE AMERICAN CHEMICAL SOCIETY
pubs.acs.org/JACS
Article

Cascade Reactions by Nitric Oxide and Hydrogen Radical for Anti-Hypoxia Photodynamic Therapy Using an Activatable Photosensitizer

Jian Sun, Xuetong Cai, Chengjun Wang, Ke Du, Weijian Chen, Fude Feng,* and Shu Wang*

Cite This: J. Am. Chem. Soc. 2021, 143, 868−878
Read Online
ACCESS | Metrics & More | Article Recommendations | Supporting Information

ABSTRACT: Organelle-targeted activatable photosensitizers are attractive to improve the specificity and controllability of photodynamic therapy (PDT), however, they suffer from a big problem in the photoactivity under both normoxia and hypoxia due to the limited diversity of phototoxic species (mainly reactive oxygen species). Herein, by effectively photocaging a π-conjugated donor−acceptor (D−A) structure with an N-nitrosamine substituent, we established a unimolecular glutathione and light coactivatable photosensitizer, which achieved its high performance PDT effect by targeting mitochondria through both type I and type II (dual type) reactions as well as secondary radicals-participating reactions. Of peculiar interest, hydrogen radical ($H^{\bullet}$) was detected by electron spin resonance technique. The generation pathway of $H^{\bullet}$ via reduction of proton and its role in type I reaction were discussed. We demonstrated that the synergistic effect of multiple reactive species originated from tandem cascade reactions comprising reduction of O_2 by $H^{\bullet}$ to form $O_2^{\bullet-}$/$HO_2^{\bullet}$ and downstream reaction of $O_2^{\bullet-}$ with $^{\bullet}NO$ to yield $ONOO^-$. With a relatively large two-photon absorption cross section for photoexcitation in the near-infrared region (166 ± 22 GM at 800 nm) and fluorogenic property, the new photosensitizing system is very promising for broad biomedical applications, particularly low-light dose PDT, in both normoxic and hypoxic environments.

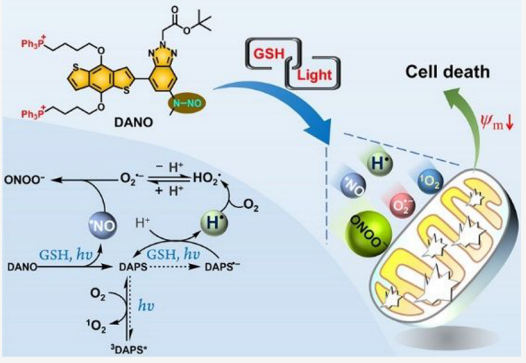

INTRODUCTION

Photodynamic therapy (PDT) is a therapeutic technique that applies a light-sensitive drug (photosensitizer, PS) and a light source to achieve selective destruction of abnormal cells, wherein the exposure of PS to light in the presence of tissue oxygen generates reactive oxygen species (ROS) and other cytotoxic free radicals. PDT has received more attention due to its unique features, including high biocompatibility, high spatiotemporal selectivity, and minimal invasiveness.[1−3] There are a variety of PSs that are clinically approved and have been successfully applied (e.g., Photofrin, acridine orange, 5-ALA, and mTHPC) for treating cancers such as skin cancers, prostate cancers, and head and neck cancers.[4] PSs are critical to the effect of PDT in tumor ablation using light to induce transient photochemical processes. Most ROS, an umbrella term of oxygen-derived short-lived intermediates reactive to biocomponents, are biorelevant in redox signaling, biosynthesis, and metabolic homeostasis and are enzymatically controlled at a dynamic and finely regulated level in living cells.[5] In the PDT effect, the photogenerated ROS in the spatially targeted area of light exposure exceeds the scavenging ability of enzymes and endogenous reductants; causes irreversible damage to proteins, lipids, and nucleic acids; and ultimately results in cell death. However, traditional PSs face a major obstacle in that they have poor therapeutic efficacy against hypoxic tumor cells, attributed to the limitation of the type II photosensitizing pathway that needs an aerobic environment to produce singlet oxygen ($^1O_2$). Simultaneously, the additional advantages that can be achieved with targeting of PSs or context-specific activation that thereby provide a dual selective effect.[6,7]

The obstacle for oxygen-dependent PSs can be overcome by a type I photosensitizing mechanism that favors the fighting of hypoxia to improve PDT through the generation of toxic free radicals such as hydroxyl radical ($^{\bullet}OH$), superoxide ion ($O_2^{\bullet-}$), and hydroperoxyl radical ($HO_2^{\bullet}$). In view of the reported examples collectively enumerated in Table S1 of the Supporting Information (SI), most of the type I reaction-based PSs are precious metallic complexes and metal-centered macrocycles,[8] on the basis of the redox photochemistry that have been intelligently evolved by nature using light harvesting capability of chlorophyll to initiate photosynthesis.[9] In contrast, the development of nonmetallic PSs that relieve the

Received: October 2, 2020
Published: January 8, 2021

https://dx.doi.org/10.1021/jacs.0c10517
J. Am. Chem. Soc. 2021, 143, 868−878

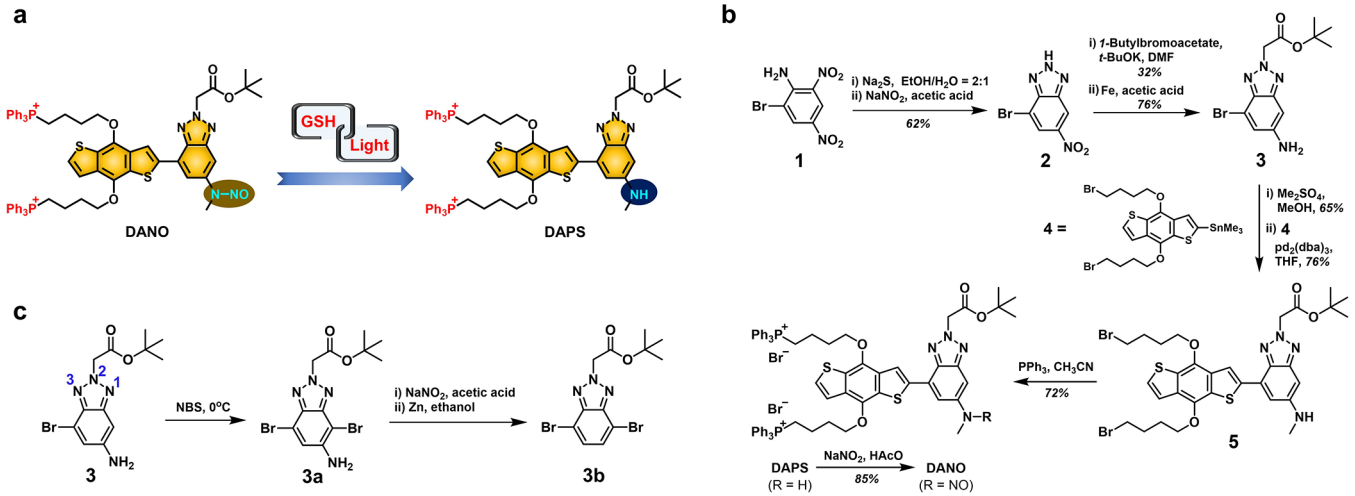

Figure 1. (a) Chemical structure of DANO and schematic illustration of GSH–light coactivation for enhanced PDT. (b) Synthetic route of DAPS and DANO. (c) Transformation of **3b** from **3** to verify the site of N-alkylation.

concerns with metal toxicity remains in its infancy in counteracting hypoxia.[10−13] Particularly, for type I reactions producing $O_2^{\bullet-}$, it is necessary to maximize the $O_2^{\bullet-}$ mediated toxicity via one or more secondary reactions that afford strongly reactive species such as peroxynitrite ($ONOO^-$) and $^{\bullet}OH$,[9] in addition to its reactivity to transition metals (e.g., reduction of iron complexes in cytochrome *c* and oxidation of iron–sulfur clusters).[14] To improve the responsive selectivity, the development of new activatable photosensitizers (aPSs) responsive to the endogenous and/or exogenous stimuli (e.g., pH, redox environment, and enzymes) is one of the most attractive strategies.[6,15] Currently, aPS molecules that enable generation of diverse reactive species, not limited to ROS, are urgently needed for efficient PDT under hypoxia. We recently reported a glutathione-hydrogen peroxide ($GSH–H_2O_2$) coresponsive benzothiadiazole-based aPS[13] that could be activated to its mature form (derived from $HO–NH_2ArSO_3H$ structurally shown in Table S1) with dual type photosensitizing capability. However, endogenous H_2O_2 is not sufficient enough for aPS activation.

In the present work, we reported an organic functional molecule, termed DANO, that possesses a π-conjugated donor–acceptor (D–A) backbone equipped with an *N*-nitrosamine substituent and two amphiphilic triphenylphosphine (TPP) ligands (Figure 1a). DANO has following important features: (1) the D–A backbone is photocaged by the *N*-nitroamine substituent, and photouncagable to liberate gaseous $^{\bullet}NO$ in a GSH dependent manner; (2) the activated DANO forms a dual type PS to effectively generate ROS (e.g., $^1O_2$ and $O_2^{\bullet-}$) as well as reactive nitrogen species (RNS) such as $^{\bullet}NO$ and peroxynitrite ($ONOO^-$); (3) upon activation of DANO by light and GSH, hydrogen radical ($H^{\bullet}$), assigned to reactive hydrogen species (RHS), is another detectable reactive intermediate, which is an extremely rare finding in PDT and adds more insight and understanding into the origination of ROS involved in type I reaction and the mechanism of multicomponent participating synergistic effects for PDT. The cascade reactions and combination of the above collective features with outstanding properties of near-infrared (NIR) two photon excitation (TPE) and imaging make DANO promising for enhanced PDT in complex tumor environments. Given that GSH is often at elevated levels in tumor cells as compared to normal cells (millimolar versus submillimolar concentrations),[16] GSH-dependent photoactivation potentially reduces the risk of nonspecific phototoxicity.

RESULTS AND DISCUSSION

Synthesis and Characterization of DANO. A compact D–A structure with maximum absorption at the blue light region is designed for this study as D–A structures have sufficient sites for flexible functionalization and feature intense intramolecular charge transfer (ICT) absorption[17] for blue light excitation as well as a TPE that is compatible with an 800 nm laser. Using benzodithiophene (BDT) and benzotriazole (BTz) as the electron donor and acceptor, respectively, we designed a conjugated BDT–BTz structure with an –N(Me)–NO substituent positioned at the BTz ring such that the whole molecule could be in a stable and deactivated state. The TPP cations are attached to the BDT moiety for localized accumulation into mitochondria which are known as one of best targets for PDT.[18]

It is noteworthy that mitochondria are less enriched with molecular oxygen as compared to the cytosol owing to the considerable oxygen consumption by the respiratory chain,[19] which necessitates type I or dual type reaction for oxygen-independent PDT. With a pK_a of 4.8,[20] $O_2^{\bullet-}$ is negatively charged at neutral pH, with the membrane impermeable and mostly confined in the mitochondrial compartment. As mitochondrial superoxide mutase (Mn-SOD) exists at high concentrations (5–20 μM)[21] and scavenges $O_2^{\bullet-}$ with an extremely high second-order reaction constant ($k = 1.2 \times 10^9$ M^{-1} s^{-1}),[22] mitochondrial $O_2^{\bullet-}$ is short-lived. However, for the case of DANO, this scavenging issue can be relieved for a couple of reasons: (1) $O_2^{\bullet-}$ reacts with $^{\bullet}NO$ to form $ONOO^-$ ($k = 6.7 \times 10^9$ M^{-1} s^{-1}), favored by the simultaneously colocalized generation of $O_2^{\bullet-}$ and $^{\bullet}NO$.[23] The slow oxidation of $^{\bullet}NO$ by O_2 can not compete with this reaction. (2) $ONOO^-$ inactivates Mn-SOD through nitration reaction,[24] which potentially suppresses SOD-catalyzed scavenging of $O_2^{\bullet-}$. Both $^1O_2$ and $ONOO^-$ are strong reactive oxygen/nitrogen species (RONS), but travel at different distance limits and target different biomacromolecules associated with mitochondrial functioning. Usually, $^1O_2$ causes lipid oxidation and selective photodamage to certain amino residues of

https://dx.doi.org/10.1021/jacs.0c10517
J. Am. Chem. Soc. 2021, 143, 868–878

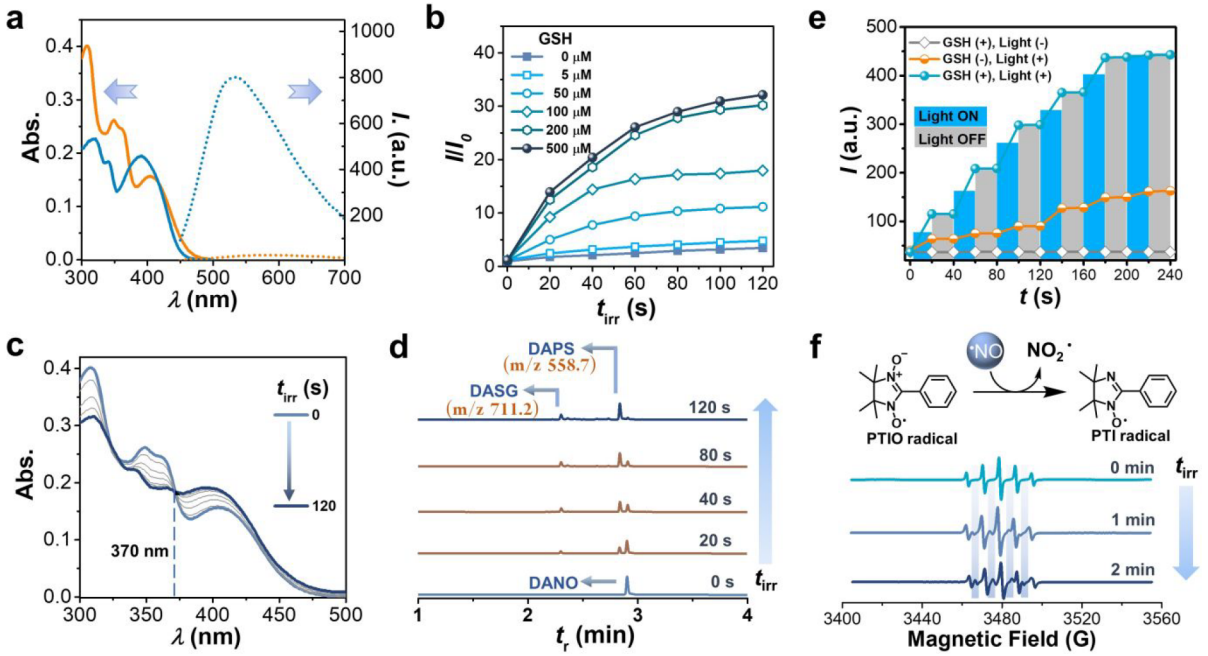

Figure 2. (a) UV−vis absorption (solid line) and fluorescence spectra (dashed line) of DANO (orange line) and DAPS (blue line) in 10% acetonitrile−PBS (pH 7.4). (b) Fluorescence enhancement (I/I_0) of the mixture containing DANO (5 μM) and GSH (0−500 μM) upon LED light irradiation at 20-s intervals. (c) UV−vis spectra and (d) UPLC analysis of solutions containing DANO (5 μM) and GSH (200 μM) upon LED light irradiation. (e) Changes of fluorescence intensity of DAF-2 solutions containing DANO (5 μM) and GSH (0 or 200 μM) with or without LED light irradiation. (f) ESR signal of the mixture containing DANO (100 μM) and PTIO (500 μM) under LED light irradiation. The reaction solvent was 10% acetonitrile−PBS (pH 7.4). Light irradiation proceeded under a 405 nm LED with a power density of 20 mW cm^{-2}.

proteins, while $ONOO^-$ induces protein nitration at tyrosine residues and oxidatively inactivates mitochondrial proteins (e.g., electron transport chain components).[25,26]

N-Nitrosoaminophenol and nitroaniline derivatives have been developed as •NO photoreleasers.[27−30] As compared to those •NO releaser−linker−reporter dyads, the −N(Me)−NO functionality of DANO has distinctive features and roles: (i) photocaging BTD−BTz backbone through photoinduced electron transfer (PET); (ii) responsive to the mutual presence of light irradiation and GSH rather than the light irradiation alone; and (iii) cascading •NO release and generation of RONS (e.g., $^1O_2$, $O_2^{\bullet-}$, and $ONOO^-$) and RHS (i.e., H•). The important role of GSH in the regulation of •NO release and the photochemical process are taken into account, which makes DANO exceptional for optimal PDT.

The synthesis of DAPS and DANO was shown in Figure 1b. The acceptor segment **3** was prepared in three steps (overall yield 15% from **1**), and coupled to the donor segment **4** via Pd(0)−catalyzed Stille reaction[31] to produce conjugated structure **5**. After substitution reaction (−Br → −TPP), DAPS was obtained. *N*-Nitrosylation reaction was carried out by treating DAPS with sodium nitrite in acetic acid to afford DANO in a yield of 85%. It should be noted that *N*-alkylation of asymmetric benzotriazole could occur at the three nitrogen positions, which raised a concern about possible impurities (i.e., isomerized forms) of key intermediate **3**. To address this issue, we treated **3** by bromination and deamination reactions and achieved the dibromo-substituted intermediate **3b** (Figure 1c) which was identified by the NMR analysis (Figure S1), thereby confirming complete *N*-alkylation at the N2 position.

Photoactivation of DANO. DANO exhibited an intense absorption band (Figure 2a) assigned to the ICT transition, peaked at 405 nm (ε_{405} = 3.1 × 10^4 M^{-1} cm^{-1}), and nearly nonfluorescent (Φ_F < 0.001 in methanol, using coumarin 307[32] with Φ_F = 0.56 in ethanol as a standard) owing to the caging effect of the *N*-nitrosamine group. DAPS absorbed maximally at 392 nm (ε_{392} = 3.9 × 10^4 M^{-1} cm^{-1}), with comparable intensity at 405 nm to DANO, which means both DANO and DAPS were compatible with a 405 nm light emitting diode (LED) for photochemical reactions. Different from DANO, DAPS was fluorogenic (Φ_F = 0.047 in PBS) and emissive maximally at 532 nm, bright enough for cell imaging purposes.

With GSH and light as stimuli factors, the uncaging process of DANO over a period of 120 s was investigated in 10% acetonitrile-phosphate saline buffer (PBS, pH 7.4). Under light (λ 405 nm, 20 mW cm^{-2}), the increase of GSH concentration (0−0.5 mM) promoted fluorescence turn-on response (Figure S2), causing fluorescence enhancement up to 30-fold (Figure 2b). The reaction kinetics was also analyzed by UV−vis absorption spectra (Figure 2c). At a fixed GSH concentration (0.2 mM), the ICT absorption band gradually blue-shifted with enhanced intensity. Interestingly, an isosbestic point appeared at 370 nm, well matching the intersection of the two absorption curves of DANO and DAPS (Figure 2a). The DANO → DAPS conversion was confirmed by ultrahigh performance liquid chromatography−mass (UPLC−MS) analysis (Figure 2d) through quantitatively monitoring the consumption of DANO and concomitant production of DAPS at the retention time (t_r) of 2.90 and 2.84 min, respectively. Evidently, the reaction was fast and rather clean, complete after 120 s of light irradiation. The only minor product was detected at t_r 2.30 min, and identified to be a GSH adduct (DASG) by the evidence of high resolution mass spectrum (HRMS, m/z 710.7332, Figure S3). However, in the absence of GSH, the conversion rate was only 12% at an irradiation time (t_{irr}) of 120

https://dx.doi.org/10.1021/jacs.0c10517
J. Am. Chem. Soc. 2021, 143, 868−878

s, without a detectable signal at t_r 2.30 min (Figure S4) as GSH was essential for the formation of the GSH adduct. In the dark, no product was detected (Figure S5).

The above results demonstrated that GSH and light could co-activate DANO by brief light irradiation within 120 s, with negligible degradation of DAPS (Figure 2d) in an aerobic photoactivation condition. To characterize the •NO photorelease property of DANO, we carried out the following experiments. First, DAF-2,[33] an •NO specific probe, was observed to fluorescently respond to the irradiation cycles applied to DANO, particularly in the presence of GSH (Figure 2e). The fluorescence intensity was plateaued after an overall t_{irr} of 100 s to indicate complete •NO release, in accord with the UPLC data (Figure 2d). Next, electron spin resonance (ESR) spectra were measured, using 2-phenyl-4,4,5,5,-tetramethylimidazoline-1-oxyl 3-oxide (PTIO radical) as a spin trapper,[34] which indicated •NO-mediated generation of PTI radical after photoreaction (t_{irr} = 1 or 2 min) (Figure 2f).

The selectivity of DANO for GSH in fluorescence response after light irradiation over a broad range of biologocally relevant species was investigated, and the results were shown in Figure 3. Only L-cysteine led to similar fluoroescence enhancement to GSH. Taking into account that GSH and L-cysteine are the most abundant intracellular thiols and the typical intracellular level of GSH (1−10 mM) is almost 1 or 2 orders of magnitude higher than that of L-cysteine (lower than 100 μM),[35−37] GSH is considered to be the most responsive thiol species to activate DANO in the living cells.

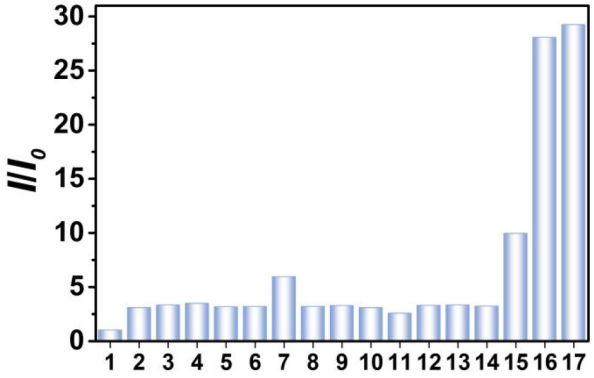

Figure 3. Fluorescence enhancement (I/I_0) of the mixture solutions containing DANO (5 μM) and different biologically relevant species (200 μM) upon LED light irradiation (1 min, λ 405 nm, 20 mW cm^{-2}). **1**: Control (DANO only in dark); **2**: DANO only in light; **3**: NO_2^-; **4**: NO_3^-; **5**: SO_3^{2-}; **6**: Fe^{3+}; **7**: Fe^{2+}; **8**: Zn^{2+}; **9**: Cu^{2+}; **10**: H_2O_2; **11**: ClO^-; **12**: Gly; **13**:Glu; **14**: Arg; **15**: NADH; **16**: Cys; and **17**: GSH.

H• Generation and Theoretical Calculation. To look more closely into the mechanism of photochemistry and roles of GSH in the photoactivation of DANO, we performed ESR spin trapping with a high concentration of 5,5-dimethyl-1-pyrroline *N*-oxide (DMPO, 500 mM) that can convert free radical intermediates into long-lived spin adducts. Interestingly, under light (t_{irr} = 1 min), the ESR signal was nearly silent in the absence of GSH, but emerged as a combination of two groups of peaks if GSH was present (Figure 4a). DMPO−H• adduct was identified according to the characteristic hyperfine splitting constants of the nine-line signal (a_N = 16.2 mT, $a_{\beta H}$ = 22.1 mT),[38] which suggested the emergence of H•. Interestingly, as the ESR data revealed, accompanied by H• generation, the carbon-centered radical was also detected by the six-line signal (a_N = 15.4 mT, $a_{\beta H}$ = 22.2 mT).[38]

We speculated that the formation of the carbon-centered radical was associated with the aniline radical resulting from the homolysis of the N−NO bond upon exposure of DANO to light and played a key role in production of DASG (i.e., the GSH adduct, detectable by UPLC−MS). Therefore, the overall photoreaction process was proposed in Figure 4b. In brief, GSH acts as a scavenger of DA1• to move forward the reversible N−NO homolysis reaction and produce the major product DAPS. The reversibility of the N−NO homolysis reaction was evidenced by the inhibition assay using NOC-13 as a NO donor (Figure S6). In another pathway, the carbon-centered radical DA2• resonated with DA1• is scavenged by GS• to form DASG in a minor quantity.

One surprising finding is the concurrent photogeneration of H•, which likely involves a proton reduction process associated with the charge separation property of D−A type materials.[39,40] The electron transfer could occur from the environment (e.g., high concentration of GSH) to the long-lived triplet excited state of DAPS (termed ^{3}DAPS*, originating from the singlet excited state, termed ^{1}DAPS*, via intersystem crossing process) and generate $DAPS^{\bullet -}$, followed by transferring one electron to proton and finally returning to the ground state of DAPS (Figure 4c). Generally, as the smallest free radical and strong reductant, the short-lived H• is immediately converted to secondary radicals or products. As DMPO captured H• at a rather high rate ($k = 3.8 \times 10^9$ M^{-1} s^{-1}),[41] the ESR measurement could be a useful tool to identify H•. Another evidence of H• generation was provided by the HRMS data (Figure S7) that indicated formation of the TEMPO adduct (m/z 158.1545) of H•. To provide further experimental evidence, we investigate the hydrogenation capability of hydrogen radical toward the aryl carbon−carbon double bond, using 4-vinylbenzoic acid (PVBA) as a substrate. As shown in Figure S8, after photoreaction of the mixture containing DANO, GSH, and PVBA, hydrogenated PVBA is detected by HR−MS with an m/z of 149.0594, in excellent consistency with the predicted value (m/z 149.0608), but it is not detectable in the control experiment lacking light irradiation. This result confirms the presence of the photogenerated hydrogen radical.

Despite the fact that H• is one of the intermediates generated by relatively harsh protocols[42−44] such as ionizing irradiation, atmospheric plasma treatment, photolysis of water by high energy UV irradiation, and photocatalysis, H• is hardly available in aqueous solutions under mild conditions. Presently, lacking controllable in situ generation methods, the reactivity of H• with cellular components is largely unkown. In living systems, H• participating reactions, such as extremely fast reduction of O_2 ($k = 2.1 \times 10^{10}$ M^{-1} s^{-1})[45] into $HO_2^\bullet$ (i.e., protonated $O_2^{\bullet -}$) should be of biological value. Highly lipophilic $HO_2^\bullet$ is detrimental to lipids by peroxidation.[46] It is noted that $O_2^{\bullet -}/HO_2^\bullet$ was not detectable when H• was depleted by excess DMPO (Figure 4a), implying that direct electron transfer between $DAPS^{\bullet -}$ and O_2 to produce $O_2^{\bullet -}/HO_2^\bullet$ in the presence of excess GSH is unfavorable but mediated by H• as follows:

$$H^\bullet + O_2 \rightarrow HO_2^\bullet \leftrightarrow H^+ + O_2^{\bullet -} \quad (1)$$

To understand the photocaging mechanism of the −NO functionality, we carried out theoretical calculations based on time-dependent density functional theory (TD-DFT) at the

https://dx.doi.org/10.1021/jacs.0c10517
J. Am. Chem. Soc. 2021, 143, 868−878

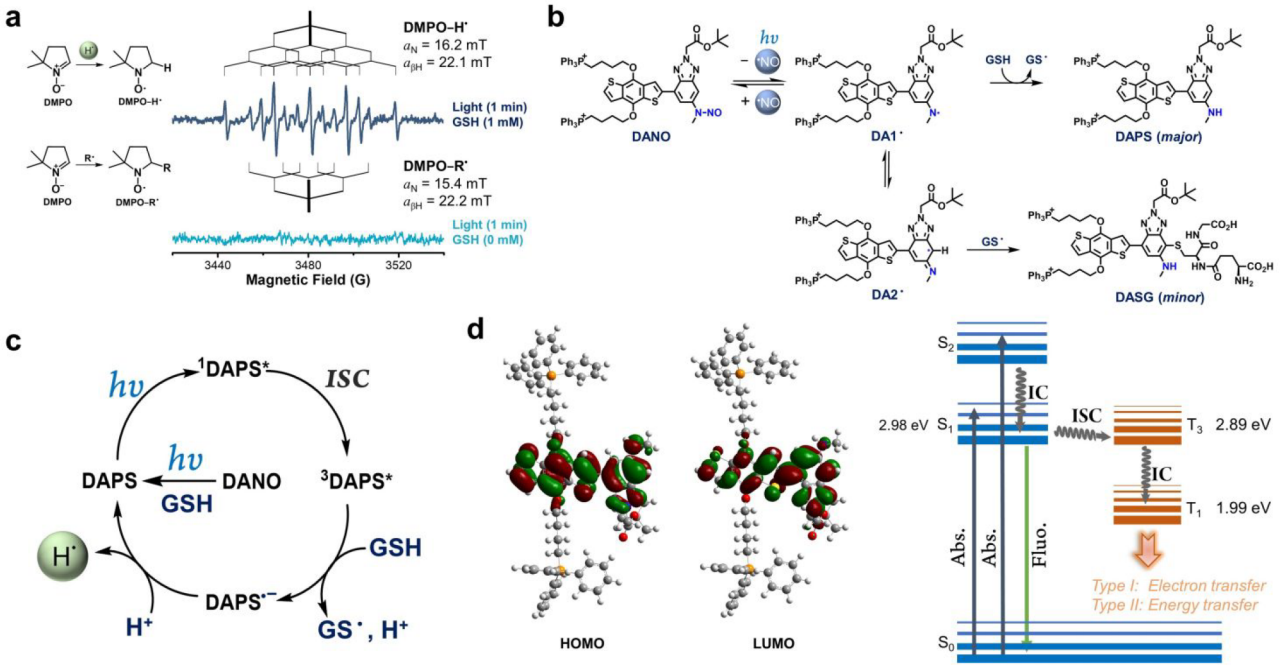

Figure 4. (a) ESR signal of the mixture containing DANO (1 mM), GSH (0 or 1 mM), and DMPO (500 mM) in 40% acetonitrile−PBS under LED light irradiation (λ 405 nm, 20 mW cm^{-2}, t_{irr} = 1 min). (b) Plausible mechanism of DANO → DAPS/DASG transformation mediated by GSH and light. (c) Proposed mechanism for the GSH-dependent photogeneration of H•. (d) Schematic diagram for frontier molecular orbitals and electronic transitions of DAPS on a basis of TD−DFT calculation.

level of B3LYP/6-31G (d) (Table S2). For DAPS, as shown in Figure 4d, the intersystem crossing (ISC) process is favorable by the small singlet−triplet energy gap (ΔE_{ST}, 0.09 eV) between S_1 and T_3 excited states, allowing the type I/type II pathway to take place. The $S_0 \rightarrow S_1$ transition (corresponding to H → L transition) is allowed with a relatively high oscillator strength (f = 0.5243), which predicts that DAPS is a fluorogenic PS. In both HOMO and LUMO orbitals, electron delocalization over the π-conjugated D−A backbone and the nitrogen atom of the −NH(Me) substituent favors photoinduced charge transfer. However, DANO is another case, associated with the addition of −NO to the −NH(Me) substituent. First, in comparison to DAPS, the dihedral angle between BDT and BTz planes is enlarged from 15.0° to 27.5°. Second, photoexcitation causes drastic electron transfer from the BDT core to the BTz plane and an N−NO bond. In the LUMO orbital, electrons are localized into the acceptor segment (Figure S9). Additionally, the H → L transition is nearly forbidden (f = 0.0008). Consequently, the N−NO bond brings electronic and structural effects by reversing the electron donating effect of the −NH(Me) substituent, facilitating the PET process, causing geometrical changes of the D−A skeleton and caging the optical properties of the conjugated structure.

Detection of RONS. Upon light irradiation, RONS including $O_2^{\bullet-}$, $^1O_2$, and $ONOO^-$ were detected by fluorescent probes or ESR-based methods. Using dihydroethidium (DHE) as a fluorescent probe for $O_2^{\bullet-}$, DAPS was shown to have stronger type I photosensitizing capability (Figure 5a) than methylene blue[11] and HO−NH_2ArSO_3H[13] (a dual type PS). Meanwhile, DAPS exhibited $^1O_2$ photosensitizing capability (Figure 5b) with a $^1O_2$ generation efficiency (Φ_Δ) of 0.42 in methanol (Figure S10), using 1,3-diphenylisobenzofuran (DPBF) as a $^1O_2$ trapper and Ru(bpy)$_3$Cl$_2$ (Φ_Δ 0.87 in methanol)[47] as an actinometer under the same light irradiation protocol (λ 435 nm, 1.5 mW cm^{-2}). The generation of $O_2^{\bullet-}$ and $^1O_2$ was also confirmed by ESR analysis (Figure 5c,d), using DMPO (500 mM) and 2,2,6,6-tetramethyl-4-piperidone (TEMP) as spin trapping agents, respectively. In contrast, the ESR signal was silent for DANO in both $O_2^{\bullet-}$ and $^1O_2$ detection. ROS such as •OH were not detected by ESR measurement (Figure S11). These results indicated that DAPS is an efficient dual type PS, with $O_2^{\bullet-}$ and $^1O_2$ as the major ROS. Comparing the DANO/GSH reaction system (Figure 4a) and DAPS alone in the presence of the same concentration of DMPO (500 mM), H• and $O_2^{\bullet-}$ adducts were detected, respectively, which was attributable to the role of excess GSH. Given the high concentration of endogenous GSH (1−10 mM) in living cells, we inffered that a cascade reaction of GSH-dependent H• and molecular oxygen accounts for the generation of $O_2^{\bullet-}/HO_2^{\bullet}$ (eq 1).

ESR measurement was not applicable to the detection of $ONOO^-$ which was a nonradical substance. Alternatively, photogenerated $ONOO^-$ in the DANO solution over a period of 120 s under light irradiation (λ 405 nm, 10 mW cm^{-2}) was detected by TPNIR-FP, an $ONOO^-$ specific probe reported by Tang et al.,[48] according to the fluorescence fluctuation at 635 nm (Figure S12). The fluorescence response was positively dependent on the GSH concentration (Figure 5e). However, the effects of excess GSH were double edged. On the one hand, GSH promoted the photoactivation of DANO to release •NO and restore DAPS, thereby substantially accelerating the formation of $ONOO^-$. On the other hand, GSH competed with TPNIR-FP in the reaction with $ONOO^-$ ($k = 5.8 \times 10^2$ M^{-1} s^{-1}),[49] which led to an underestimation of the level of generated $ONOO^-$.

To conclude, the photouncaging of DANO is coactivatable by light irradiation and GSH, and DAPS is a PS effective in a dual type mechanism. The interplay of H• and O_2 opens a

https://dx.doi.org/10.1021/jacs.0c10517
J. Am. Chem. Soc. 2021, 143, 868−878

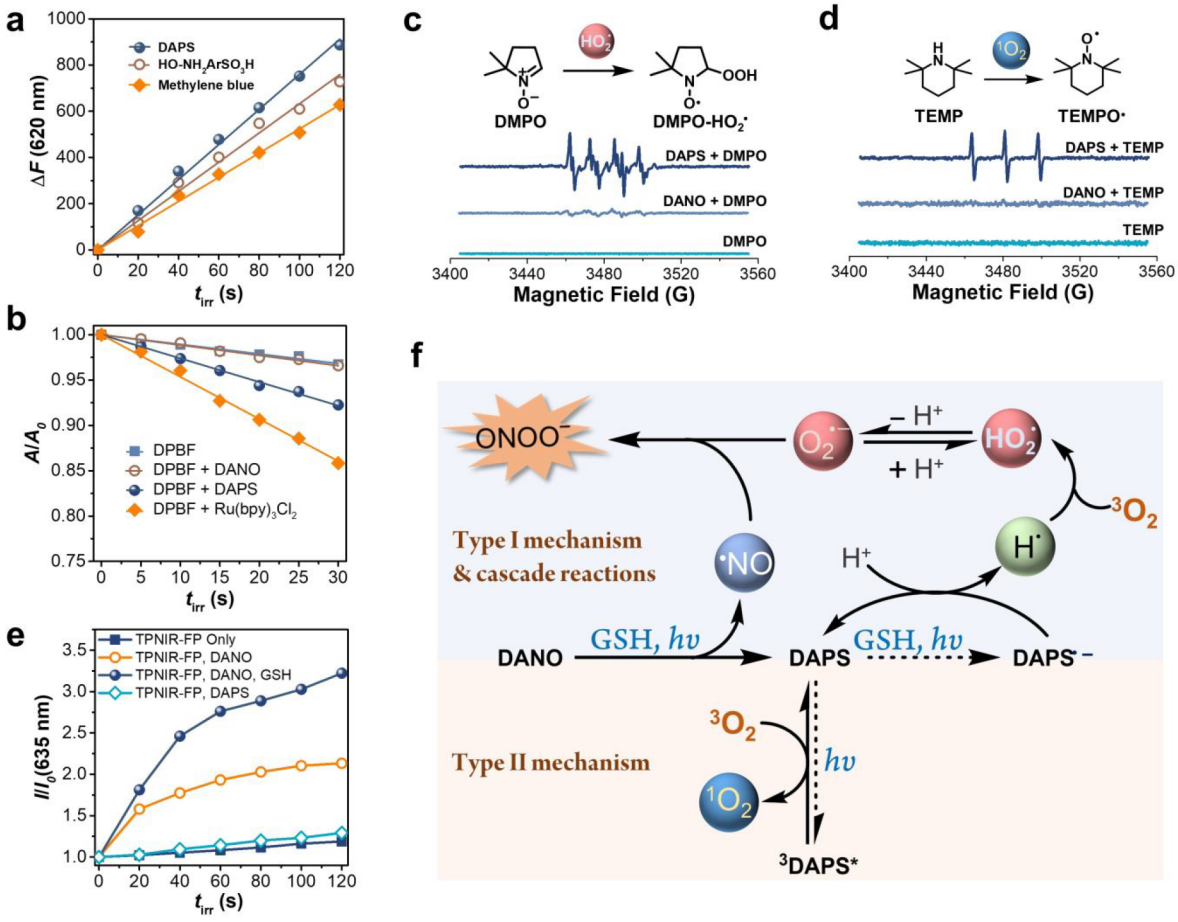

Figure 5. (a) The plot of fluorescence fluctuation (ΔF) of DHE at 620 nm versus t_{irr}. The LED light power density was 10 mW cm^{-2}, and the irradiation wavelengths were 405, 405, and 635 nm for DAPS, HO−NH_2ArSO_3H, and methylene blue, respectively. The concentration of each photosensitizer was 5 μM. (b) The plot of A/A_0 of DPBF versus t_{irr}, where A and A_0 denoted absorption intensity at 410 nm before and after light irradiation, respectively. LED light irradiation (λ 435 nm, 1.5 mW cm^{-2}) was used. ESR spectra for the detection of (c) $O_2^{\bullet-}$ and (d) $^1O_2$ using DMPO (in DMSO) and TEMP (in H_2O) as spin trapping probes, respectively. (e) Fluorescence enhancement of the mixture containing TPNIR-FP (ONOO$^-$ probe) and indicated substrates after LED light irradiation (λ 405 nm, 20 mW cm^{-2}, t_{irr} = 0−120 s). (f) Schematic illustration of the photogeneration of H$^\bullet$, $O_2^{\bullet-}$/$HO_2^\bullet$, $^\bullet$NO, ONOO$^-$, and $^1O_2$ by coactivation of DANO with GSH and light.

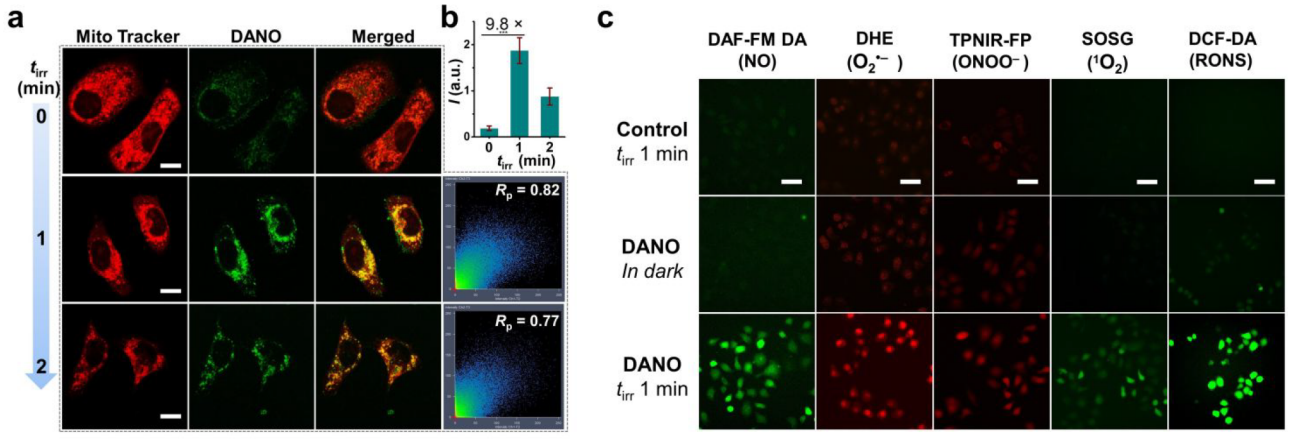

Figure 6. (a) CLSM images of DANO-treated HeLa cells after LED light irradiation (λ 405 nm, 20 mW cm^{-2}, t_{irr} = 0, 1 and min). The cells were stained with Mito Red Tracker. Scale bars, 10 μm. (b) The median fluorescence intensities derived from images in a. Statistical significance was assessed using a two-way analysis of variance test (**$P \leq 0.05$, ***$P \leq 0.001$). (c) Fluorescence images of intracellular RONS. Scale bars, 50 μm.

door for a cascade of $^\bullet$NO and $O_2^{\bullet-}$ to generate ONOO$^-$. The schematic diagram of networked ROS/RNS/RHS generation pathways was concisely illustrated in Figure 5f.

Intracellular Activation of DANO and Phototoxicity. The activation process was investigated by imaging the living cells with confocal laser scanning microscopy (CLSM). HeLa cells were treated with DANO (5 μM) for 2 h, washed, and

https://dx.doi.org/10.1021/jacs.0c10517
J. Am. Chem. Soc. 2021, 143, 868−878

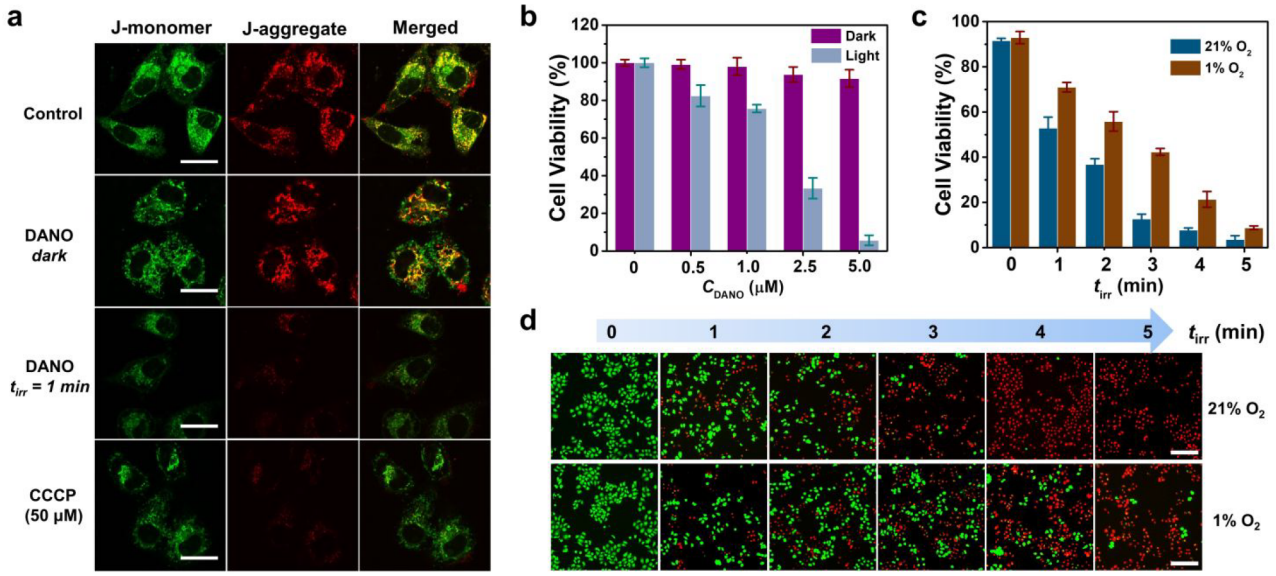

Figure 7. (a) CLSM images of HeLa cells treated with DANO (0 or 5 μM) after LED light irradiation (t_{irr} = 0 or 1 min) or treated with CCCP. The cells were stained with JC-1. Scale bars: 10 μm. (b) Viabilities of HeLa cells treated with varied concentrations of DANO (0−5 μM) 24 h after LED light irradiation (t_{irr} = 0 or 4 min). (c) Viabilities of HeLa cells treated with DANO (5 μM) under 21% or 1% O_2 condition, 24 h after LED light irradiation (t_{irr} = 0−5 min). (d) Fluorescence imaging of DANO (5 μM)-treated HeLa cells after LED light irradiation (t_{irr} = 0−5 min). The live and dead cells were stained by Calcein-AM and PI, respectively. Scale bars, 100 μm.

received brief light irradiation (λ 405 nm, 1.5 mW cm^{-2}). The mitochondria were stained with Mito Tracker Red. DAPS could be detected by its green fluorescence collected at 470−540 nm ranges with excitation at 405 nm. As compared to the dim fluorescence of the control group (t_{irr} = 0 min), the irradiated cells (t_{irr} = 1 min) emitted bright green fluorescence with a Pearson's overlap coefficient (R_p) of 0.82 (Figure 6a,b), which indicated successful activation of DANO in mitochondria by a low dose of light (1.2 J cm^{-2}). Using Mito Tracker Red as a fluorescent indicator, it seems the mitochondrial membrane of DANO-treated cells was destabilized after 1−2 min of light irradiation. The GSH-responsive property of DANO was investigated using L-buthionine-(S,R)-sulfoximine (BSO) as a GSH depletor. As shown in Figure S13, treatment by BSO (10 μM) led to a decrease of fluorescence intensity in the DANO-treated cells upon light irradiation (t_{irr} 1 min, λ 405 nm, 20 mW cm^{-2}) by ~25%, in agreement with the GSH-dependent activation manner of DANO.

Note that a relatively longer irradiation time (t_{irr} = 2 min) would decrease the fluorescence intensity but increase the cytotoxicity of DANO. This observation could be interpreted by the effect of mitochondria-targeting PDT, according to the morphological changes of mitochondria from a tubular state (favorable for staining) to a fragmented state (not favorable for staining) (Figure 6a), which was well consistent with the previous report of PDT by modulation of the mitochondrial morphology.[50] The light irradiation activated DANO and caused liberation of highly cytotoxic species that led to leakage of fluorescent molecules and affected the integrity of mitochondrial membrane structures and also probably the cell membrane, as previously revealed by Zhao et al.[51] As a result, the fluorescence channels from both the Mitotracker and the fluorescent product by activating DANO showed reduced intensity (t_{irr} = 2 min).

To assess the intracellular RONS level, we detected primary RONS using DAF-FM DA, DHE, singlet oxygen sensor green (SOSG, cell permeable in standard maintenance medium buffer),[52] and TPNIR-FP as fluorescent probes for $^{\bullet}$NO, $O_2^{\bullet-}$, $^1O_2$, and $ONOO^-$, respectively. As a result, DANO-treated cells in the dark showed similar fluorescence intensity to the background signal (Figure 6c), however, responding to light irradiation (t_{irr} = 1 min) with enhanced fluorescence that indicated the respective existence of photogenerated RONS. The level of total intracellular RONS was reflected by the elevated fluorescence signal using 2,7-dichlorofluorescein diacetate (DCFH-DA) as a nonspecific probe. These results revealed that the photoactivation of DANO in the living cells was successful and multiple toxic RONS were generated, thanks to the effective type I and type II reactions secondary to photorelease of $^{\bullet}$NO. Particularly, the detected signals of $O_2^{\bullet-}$ and $ONOO^-$ conveyed a message that the H$^{\bullet}$ and $^{\bullet}$NO cascade reactions could occur in the living system, which provides a foundation for synergistic antihypoxia PDT.

Depolarization of the mitochondrial membrane is one of leading pathways for mitochondria-localized PS to induce cell apoptosis.[53] To evaluate the effect of photoexcited DANO on mitochondria, we examined the changes of the mitochondrial membrane potential (MMP, ψ_m) with commercial dye JC-1 as a $\Delta\psi_m$ indicator by comparing the emission signals of J-monomer (in the green channel, predominantly distributed in cytosol) and J-aggregates (in the red channel, located in intact mitochondrial membrane) under CLSM. In the dark, bright red fluorescence was detected in DANO-treated cells, in a similar pattern to the control experiment (Figure 7a). The intensity of red fluorescence was sharply attenuated in the DANO-treated cells exposed to blue LED light (λ 405 nm, 20 mW cm^{-2}, t_{irr} = 1 min).

The photodamage effect was comparable to the effect of CCCP (a mitochondria membrane disrupter).[54] The prompt changes of ψ_m were attributable to the permeabilization of the mitochondrial membrane, induced by the effect of locally generated ROS on the mitochondrial components such as the permeability transition pore complex (PTPC) including a voltage-dependent anion channel (VDAC, the most abundant

https://dx.doi.org/10.1021/jacs.0c10517
J. Am. Chem. Soc. 2021, 143, 868−878

mitochondrial outer membrane protein) and adenine nucleotide translocator (ANT, the most abundant mitochondrial inner membrane protein).[55] For example, ANT is extremely sensitive to $^1O_2$-mediated oxidation at the thiol groups responsive for nucleotide transport and opening of the permeability transition pore.[56] Peroxidation of unsaturated lipids by excess RONS (e.g., $^1O_2$, $HO_2^\bullet$ and $ONOO^-$)[57] can also induce mitochondrial dysfunction and ψ_m disruption. The combined effect of RONS tends to impair a broad spectrum of critical mitochondrial targets.

To investigate the in vitro PDT performance of DANO, we carried out MTT assay 24 h after treatment of HeLa cells with DANO over various periods of light irradiation (λ 405 nm, 20 mW cm^{-2} for 0−5 min). The dark toxicity of DANO (0−5 μM) was low (Figure 7b). Light irradiation (t_{irr} = 4 min) of DANO- treated cells caused decreased viabilities, strickingly reducing the viability to only 6% in the presence of 5 μM DANO. The phototoxicity was also dependent on the light fluence (0−6 J cm^{-2}) and oxygen concentration (Figures 7c and S14). Although the PDT effect was more favored under 21% O_2 than 1% O_2 because of $^1O_2$ generation, the cell killing performance under 1% O_2 (only 9% cell survival; 6 J cm^{-2}) was comparable to or prevailing over the most reported PDT agents shown in Table S1. The PDT effect under 21% O_2 and 1% O_2 was also verified by the live/dead cell staining assay (Figures 6d and S15) which recognized dead cells (in red) from live cells (in green), highlighting the excellent PDT performance of activated DANO under both normoxia and hypoxia. DAPS exhibited significant phototoxicity under both normoxia and hypoxia (Figure S16), thanks to its photosensitizing capability through the dual type pathway. However, the PDT effect was lower than DANO.

In Vitro Two-Photon Imaging and PDT. Two-photon property is attractive for aPSs by excitation in an NIR window and localized region with improved penetration depth. With a D−A conjugated backbone contributable to two-photon absorption,[58] DAPS exhibited a large δ value of 166 ± 22 GM at 800 nm (in methanol, using rhodamine 6G as a reference[59]). To make sure of the two-photon photoactivation with DANO, we loaded DANO solution containing 0 or 200 μM GSH into a glass capillary[60] (0.3 mm in diameter) for irradiation by an 800 nm two-photon laser (Figure 8a). DANO could be coactivated by GSH and two-photon light (t_{irr} = 30 s) in a response of upconversion fluorescence that showed generation of DAPS (Figure 8b). This feature would bring great convenience for cell studies. Actually, under two-photon CLSM, the bright fluorescence signal clearly detected in the cells pretreated with DANO and LED light could visualize the localization of fluorogenic DAPS in cytosolic vesicles (Figure 8c). According to the live/dead staining assay (Figure 8d), tumor cells in the two-photon beam focused region could be eradicated after very brief laser irradiation (1 or 2 min). Therefore, DANO is perfectly compatible with two-photon excited PDT.

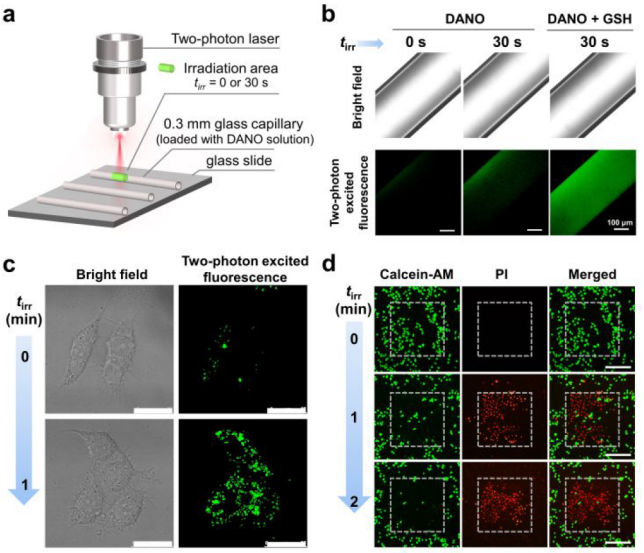

Figure 8. (a) Representation of activation of DANO loaded in glass capillary under two-photon excitation. (b) Two-photon fluorescence images of a DANO-loaded glass capillary in the absence or presence of GSH (200 μM) after two-photon laser irradiation (λ 800 nm, t_{irr} = 0 or 30 s). (c) Two-photon fluorescence images of DANO (5 μM)-treated HeLa cells after LED light irradiation (λ 405 nm, 20 mW cm^{-2}, t_{irr} = 0 or 1 min). Scale bars, 10 μm. (d) Fluorescence imaging of DANO (5 μM)-treated HeLa cells after two-photon laser irradiation (λ 800 nm, t_{irr} = 0, 1, or 2 min). The gray dashed square in each image indicates the laser irradiation area (435 × 435 μm^2). Scale bars, 200 μm.

CONCLUSIONS

In summary, we designed nonmetallic DANO as a stimuli-responsive aPS by coupling a $^\bullet$NO photogenerator to a light-harvesting conjugated D−A structure. The advantages of DANO for PDT are multifold: (1) the small N(Me)−NO substituent has a substantial photocaging effect on the optical properties of D−A motif via photoinduced electron transfer; (2) the uncaging process is mutually controllable by GSH and blue light to activate multiple photochemical reactions secondary to $^\bullet$NO release; (3) the dually effective photoreaction pathways (type I and type II) enable photogeneration of reactive O/N/H species such as $^1O_2$, $O_2^{\bullet-}/HO_2^\bullet$, $ONOO^-$, and H$^\bullet$; (4) DANO targets mitochondria and exhibits excellent in vitro PDT performance under both normoxia (21% O_2) and hypoxia (1% O_2) by inducing apoptosis of tumor cells (<10% cell viability) at a very low dose of light up to 6 J cm^{-2}; and (5) efficient two-photon excited PDT with DANO as an aPS is also achievable using the widely accepted 800 nm two-photon laser. Taken together, as compared to other reported aPS materials, DANO is a high-performance unimolecular aPS to locally generate a combination of short-lived reactive species, paving a way to break the bottleneck of hypoxia-limited PDT.

Presently, careful studies on the detection and role of H$^\bullet$ in a type I reaction mechanism for PDT remain to be explored. Using DMPO as the H$^\bullet$ scavenger and probe, ESR evidence revealed the existence of short-lived H$^\bullet$ as well as the relationship between H$^\bullet$ and $O_2^{\bullet-}/HO_2^\bullet$. The hypothesis of H$^\bullet$-dependent $O_2^{\bullet-}/HO_2^\bullet$ generation pathway for organic dye-based type I photosensitization provides an alternative view to look into the electron transfer process during GSH-participating photochemical reactions. The closely linked cascade free radical reaction systems, such as a cascade of H$^\bullet$ and O_2 to form $O_2^{\bullet-}/HO_2^\bullet$, and a cascade of $O_2^{\bullet-}$ and $^\bullet$NO to form $ONOO^-$, highlights the utmost position of H$^\bullet$ at the upstream of cascade reactions. Definitely, the multilevel synergistic interplay among ROS, RNS, RHS, and even reactive sulfur species (RSS, not limited to GSH and GS$^\bullet$) can potentially augment antitumor therapeutic outcomes.

https://dx.doi.org/10.1021/jacs.0c10517
J. Am. Chem. Soc. 2021, 143, 868−878

EXPERIMENTAL SECTION

Synthetic Methods. *DAPS.* To a solution of **5** (150 mg, 0.2 mmol) in acetonitrile (10 mL) was added triphenylphosphine (524 mg, 2 mmol) under argon atmosphere. The reaction solution was stirred at 85 °C for 36 h and concentrated in vacuo. Silica-gel column chromatography using dichloromethane/methanol (10:1) as eluent afforded DAPS (184 mg, 72%) as a yellow solid; ^{1}H NMR (400 MHz, CD_3CN): δ 8.38 (s, 1H), 7.84−7.65 (m, 30H), 7.56 (s, 1H), 7.50 (d, J = 4.45 Hz, 1H), 7.38 (d, J = 4.45 Hz, 1H), 6.64 (s, 1H), 5.37 (s, 2H), 4.38 (m, 4H), 3.44 (m, 4H), 2.88 (s, 3 H), 2.10 (m, 4H), 1.93 (m, 4H), 1.46 (s, 9H) ppm; ^{13}C NMR (100 MHz, CD_3CN): δ 166.2, 139.3, 147.6, 144.2, 143.6, 139.4, 135.0, 133.7, 131.3, 131.2, 130.3, 130.2, 130.1, 129.2, 127.3, 120.3, 120.0, 119.6, 117.9, 117.4, 89.9, 82.9, 72.9, 72.8, 57.3, 31.0, 30.9, 30.8, 29.6, 27.2, 21.8, 21.7, 21.4, 21.3, and 19.3 ppm. HRMS (ESI+): m/z 558.1997 $[M\text{-}2Br]^{2+}$, calculated for $[C_{67}H_{66}N_4O_4P_2S_2]^{2+}$: 558.1995; found 558.1997.

DANO. To a solution of DAPS (128 mg, 0.1 mmol) in 9:1 (v/v) mixture of dichloromethane and acetic acid (10 mL) was added $NaNO_2$ (1.03 g, 15 mmol) at 0 °C. The reaction was stirred at 25 °C for 1 h and neutralized with saturated $NaHCO_3$ aqueous solution. The mixture solution was extracted with chloroform (20 mL × 3) and concentrated in vacuo. Silica-gel column chromatography using CH_2Cl_2/MeOH (7:1) as eluent afforded DANO (110 mg, 85%) as a yellow solid; ^{1}H NMR (400 MHz, CD_3CN): δ 8.43 (s, 1H),8.03 (s, 1H), 7.84−7.64 (m, 31H), 7.50 (d, J = 4.45 Hz, 1H), 7.32 (d, J = 4.45 Hz, 1H), 5.57 (s, 2H), 4.33 (m, 4H), 3.50 (s, 3H), 3.49 (m, 4H), 2.08 (m, 4H),1.91 (m, 4H), 1.46 (s, 9H) ppm; ^{13}C NMR (100 MHz, CD_3CN): δ 166.8, 145.1, 144.5, 143.4, 135.1, 133.8, 133.7, 131.7, 131.1, 130.3, 130.2, 128.8, 127.8, 121.9, 120.3, 117.9, 117.4, 106.4, 83.4, 73.0, 72.6, 58.3, 31.3, 30.9, 30.7, 27.3, 21.6, 21.5, 19.4, and 19.3 ppm. HRMS (ESI+): m/z 572.6954 $[M\text{-}2Br]^{2+}$, calculated for $[C_{67}H_{65}N_5O_5P_2S_2]^{2+}$: 572.6946; found 572.6954.

ESR Measurements. Electron spin resonance (ESR) measurements were carried out on a Bruker EMX 10/12 instrument equipped with a TE-mode cavity. A thin-walled quartz sample tube (Bruker) was used as the reaction vessel. The ESR settings were described as follows: modulation frequency 100 kHz, microwave power 20 mW, center field 3480 G, sweep width 200 G, scan time, 2 min. Spin trapping agents DMPO, PTIO, and TEMP were applied to identify the relevant radical in suitable solvents. The prepared solutions were irradiated at 298 K directly in ESR resonator using an LED lamp (405 nm, 20 mW cm^{-2}). After irradiation, the ESR spectra were recorded and further analyzed by Bruker software Win EPR.

Computational Analysis. All calculations were performed using the Gaussian 09 program package. The geometries of DANO and DAPS were optimized using DFT/B3LYP/6-31G(d). The excitation energies for the singlet and triplet excited states of DANO and DAPS were predicted using TD-DFT/B3LYP/6-31G(d) based on the optimized structure in acetonitrile.

Cell Viability Assays under Normoxia and Hypoxia. HeLa cells were seeded in the 96 well plate at a density of 2 × 10^5 cells per well and cultured for 24 h. The cells were treated with fresh growth medium containing DANO (5 μM) for 2 h under 21% O_2 or 1% O_2 atmosphere, followed by exposure to light irradiation for 0−5 min with an LED lamp (λ 405 nm, 20 mW cm^{-2}) and incubation for an additional 24 h in dark. After washing twice with PBS, freshly prepared MTT solution (100 μL, 0.5 mg mL^{-1}) was added to each well and incubated for 4 h. After removal of the supernatant, DMSO (150 μL per well) was added to dissolve the produced formazan and shaken for 10 min. The $OD_{450\ nm}$ value of each well was recorded with a Tecan multimode microplate reader to calculate the cell viability.

For dead/live cell costaining, the cells were treated in the same procedure except that the MTT solution was replaced with the solution of Calcein-AM (1.6 μg mL^{-1}) and propidium iodide (PI, 1.6 μg mL^{-1}) in PBS. Then the cells were incubated for an additional 20 min. After multiple rinses with PBS, the cells were imaged by an inverted fluorescent microscope.

Two-Photon Imaging and Excited Photodynamic Therapy. HeLa cells were seeded in 24 well plates at a density of 5 × 10^5 cells per well and incubated for 24 h. After incubation with DANO (5 μM) in fresh growth medium, the cells were irradiated for 1 min with an LED lamp (λ 405 nm, 20 mW cm^{-2}). Two-photon imaging experiments were performed on a Leica TCS SP5 laser scanning microscope with a 40× objective lens, using an 800 nm Ti-Sapphire laser (~10 W at 800 nm; ~1% average power in the focal plane). The upconversion emission was collected at 470−550 nm ranges.

For the two-photon excited PDT experiment, DANO-treated cells were irradiated within a 435 × 435 μm^2 focal area by the 800 nm TP laser (~100 mW) for different scanning time (0, 60, and 120 s), and incubated for additional 4 h, followed by addition of calcein-AM (1.6 μg mL^{-1}) and PI (1.6 μg mL^{-1}) in PBS. The cells were incubated for 20 min. After washing by PBS three times, the cells were imaged by an inverted fluorescent microscope. The living and dead cells were visualized in green and red fluorescence, respectively.

ASSOCIATED CONTENT

Supporting Information

The Supporting Information is available free of charge at https://pubs.acs.org/doi/10.1021/jacs.0c10517.

Detailed materials, instrumentation, syntheses of **2**−**5**, NMR spectra, and supporting figures and tables (PDF)

AUTHOR INFORMATION

Corresponding Authors

Fude Feng − *Department of Polymer Science & Engineering, School of Chemistry & Chemical Engineering, Nanjing University, Nanjing 210023, P. R. China;* orcid.org/0000-0002-5348-5959; Email: fengfd@nju.edu.cn

Shu Wang − *Beijing National Laboratory for Molecular Sciences, Key Laboratory of Organic Solids, Institute of Chemistry, Chinese Academy of Sciences, Beijing 100190, P. R. China;* orcid.org/0000-0001-8781-2535; Email: wangshu@iccas.ac.cn

Authors

Jian Sun − *Department of Polymer Science & Engineering, School of Chemistry & Chemical Engineering, Nanjing University, Nanjing 210023, P. R. China*

Xuetong Cai − *Department of Polymer Science & Engineering, School of Chemistry & Chemical Engineering, Nanjing University, Nanjing 210023, P. R. China*

Chengjun Wang − *School of Chemistry and Chemical Engineering, Southeast University, Nanjing 211189, P. R. China*

Ke Du − *Department of Polymer Science & Engineering, School of Chemistry & Chemical Engineering, Nanjing University, Nanjing 210023, P. R. China*

Weijian Chen − *Department of Polymer Science & Engineering, School of Chemistry & Chemical Engineering, Nanjing University, Nanjing 210023, P. R. China; Beijing National Laboratory for Molecular Sciences, Key Laboratory of Organic Solids, Institute of Chemistry, Chinese Academy of Sciences, Beijing 100190, P. R. China*

Complete contact information is available at: https://pubs.acs.org/10.1021/jacs.0c10517

Notes

The authors declare no competing financial interest.

ACKNOWLEDGMENTS

We thank the National Key R&D Program of China (2017YFA0701301, 2018YFE0200700), National Natural Science Foundation of China (22077065, 22021002,

22020102005), and Program for Changjiang Scholars and Innovative Research Team in University for financial support.

REFERENCES

(1) Celli, J. P.; Spring, B. Q.; Rizvi, I.; Evans, C. L.; Samkoe, K. S.; Verma, S.; Pogue, B. W.; Hasan, T. Imaging and Photodynamic Therapy: Mechanisms, Monitoring, and Optimization. *Chem. Rev.* **2010**, *110*, 2795−2838.
(2) Cao, H. Q.; Wang, L.; Yang, Y.; Li, J.; Qi, Y. F.; Li, Y.; Li, Y.; Wang, H.; Li, J. B. An Assembled Nanocomplex for Improving both Therapeutic Efficiency and Treatment Depth in Photodynamic Therapy. *Angew. Chem., Int. Ed.* **2018**, *57*, 7759−7763.
(3) Lovell, J. F.; Liu, T. W.; Chen, J.; Zheng, G. Activatable Photosensitizers for Imaging and Therapy. *Chem. Rev.* **2010**, *110*, 2839−2857.
(4) Singh, S.; Aggarwal, A.; Bhupathiraju, N. V. S. K.; Arianna, G.; Tiwari, K.; Drain, C. M. Glycosylated Porphyrins, Phthalocyanines, and Other Porphyrinoids for Diagnostics and Therapeutics. *Chem. Rev.* **2015**, *115*, 10261−10306.
(5) Sies, H.; Jones, D. P. Reactive oxygen species (ROS) as pleiotropic physiological signalling agents. *Nat. Rev. Mol. Cell Biol.* **2020**, *21*, 363−383.
(6) Dolmans, D.; Fukumura, D.; Jain, R. K. Photodynamic therapy for cancer. *Nat. Rev. Cancer* **2003**, *3*, 380−387.
(7) Li, X.; Kolemen, S.; Yoon, J.; Akkaya, E. U. Activatable photosensitizers: agents for selective photodynamic therapy. *Adv. Funct. Mater.* **2017**, *27*, 1604053.
(8) Wang, Y.; Liu, Y.; Sun, H.; Guo, D. Type I photodynamic therapy by organic−inorganic hybrid materials: From strategies to applications. *Coord. Chem. Rev.* **2019**, *395*, 46−62.
(9) Croce, R.; van Amerongen, H. Natural strategies for photosynthetic light harvesting. *Nat. Chem. Biol.* **2014**, *10*, 492−501.
(10) Li, M.; Xia, J.; Tian, R.; Wang, J.; Fan, J.; Du, J.; Long, S.; Song, X.; Foley, J. W.; Peng, X. Near-Infrared Light-Initiated Molecular Superoxide Radical Generator: Rejuvenating Photodynamic Therapy against Hypoxic Tumors. *J. Am. Chem. Soc.* **2018**, *140*, 14851−14859.
(11) Li, X.; Lee, D. J.; Huang, D.; Yoon, J. Phthalocyanine-assembled nanodots as photosensitizers for highly efficient type I photoreactions in photodynamic therapy. *Angew. Chem., Int. Ed.* **2018**, *57*, 9885−9890.
(12) Nguyen, V.; Qi, S.; Kim, S.; Kwon, N.; Kim, G.; Yim, Y.; Park, S.; Yoon, J. An Emerging Molecular Design Approach to Heavy-Atom-Free Photosensitizers for Enhanced Photodynamic Therapy under Hypoxia. *J. Am. Chem. Soc.* **2019**, *141*, 16243−16248.
(13) Sun, J.; Du, K.; Diao, J.; Cai, X.; Feng, F.; Wang, S. GSH and H_2O_2 Co-Activatable Mitochondria-Targeted Photodynamic Therapy under Normoxia and Hypoxia. *Angew. Chem., Int. Ed.* **2020**, *59*, 12122−12128.
(14) D'Autréaux, B.; Toledano, M. B. ROS as signalling molecules: mechanisms that generate specificity in ROS homeostasis. *Nat. Rev. Mol. Cell Biol.* **2007**, *8*, 813−824.
(15) Luby, B. M.; Walsh, C. D.; Zheng, G. Advanced Photosensitizer Activation Strategies for Smarter Photodynamic Therapy Beacons. *Angew. Chem., Int. Ed.* **2019**, *58*, 2558−2569.
(16) Malla, J. A.; Umesh, R. M.; Yousf, S.; Mane, S.; Sharma, S.; Lahiri, M.; Talukdar, P. A Glutathione Activatable Ion Channel Induces Apoptosis in Cancer Cells by Depleting Intracellular Glutathione Levels. *Angew. Chem., Int. Ed.* **2020**, *59*, 7944−7952.
(17) Sun, J.; Li, X.; Du, K.; Feng, F. A water soluble donor−acceptor−donor conjugated oligomer as a photosensitizer for mitochondria-targeted photodynamic therapy. *Chem. Commun.* **2018**, *54*, 9194−9197.
(18) Zielonka, J.; Joseph, J.; Sikora, A.; Hardy, M.; Ouari, O.; Vasquez-Vivar, J.; Cheng, G.; Lopez, M.; Kalyanaraman, B. Mitochondria-Targeted Triphenylphosphonium-Based Compounds: Syntheses, Mechanisms of Action, and Therapeutic and Diagnostic Applications. *Chem. Rev.* **2017**, *117*, 10043−10120.
(19) Turrens, J. F. Superoxide Production by the Mitochondrial Respiratory Chain. *Biosci. Rep.* **1997**, *17*, 3−8.
(20) Bielski, B. H. J.; Allen, A. O. Mechanism of the disproportionation of superoxide radicals. *J. Phys. Chem.* **1977**, *81*, 1048−1051.
(21) Radi, R. Oxygen radicals, nitric oxide, and peroxynitrite: Redox pathways in molecular medicine. *Proc. Natl. Acad. Sci. U. S. A.* **2018**, *115*, 5839−5848.
(22) Sheng, Y.; Abreu, I. A.; Cabelli, D. E.; Maroney, M. J.; Miller, A.; Teixeira, M.; Valentine, J. S. Superoxide Dismutases and Superoxide Reductases. *Chem. Rev.* **2014**, *114*, 3854−3918.
(23) Huie, R. E.; Padmaja, S. The Reaction of NO With Superoxide. *Free Radical Res. Commun.* **1993**, *18*, 195−199.
(24) Pacher, P.; Beckman, J. S.; Liaudet, L. Nitric Oxide and Peroxynitrite in Health and Disease. *Physiol. Rev.* **2007**, *87*, 315−424.
(25) Ferrer-Sueta, G.; Campolo, N.; Trujillo, M.; Bartesaghi, S.; Carballal, S.; Romero, N.; Alvarez, B.; Radi, R. Biochemistry of Peroxynitrite and Protein Tyrosine Nitration. *Chem. Rev.* **2018**, *118*, 1338−1408.
(26) Di Mascio, P.; Martinez, G. R.; Miyamoto, S.; Ronsein, G. E.; Medeiros, M. H. G.; Cadet, J. Singlet Molecular Oxygen Reactions with Nucleic Acids, Lipids, and Proteins. *Chem. Rev.* **2019**, *119*, 2043−2086.
(27) Ieda, N.; Hotta, Y.; Miyata, N.; Kimura, K.; Nakagawa, H. Photomanipulation of Vasodilation with a Blue-Light-Controllable Nitric Oxide Releaser. *J. Am. Chem. Soc.* **2014**, *136*, 7085−7091.
(28) Fraix, A.; Sortino, S. Combination of PDT photosensitizers with NO photodononors. *Photochem. Photobiol. Sci.* **2018**, *17*, 1709−1727.
(29) Zhou, E. Y.; Knox, H. J.; Reinhardt, C. J.; Partipilo, G.; Nilges, M. J.; Chan, J. Near-Infrared Photoactivatable Nitric Oxide Donors with Integrated Photoacoustic Monitoring. *J. Am. Chem. Soc.* **2018**, *140*, 11686−11697.
(30) Zhang, Z.; Wu, J.; Shang, Z.; Wang, C.; Cheng, J.; Qian, X.; Xiao, Y.; Xu, Z.; Yang, Y. Photocalibrated NO Release from N-Nitrosated Napthalimides upon One-Photon or Two-Photon Irradiation. *Anal. Chem.* **2016**, *88*, 7274−7280.
(31) Patel, D. G.; Feng, F.; Ohnishi, Y.; Abboud, K. A.; Hirata, S.; Schanze, K. S.; Reynolds, J. R. It Takes More Than an Imine: The Role of the Central Atom on the Electron-Accepting Ability of Benzotriazole and Benzothiadiazole Oligomers. *J. Am. Chem. Soc.* **2012**, *134*, 2599−2612.
(32) Reynolds, G. A.; Drexhage, K. H. New coumarin dyes with rigidized structure for flashlamp-pumped dye lasers. *Opt. Commun.* **1975**, *13*, 222−225.
(33) Kojima, H.; Nakatsubo, N.; Kikuchi, K.; Kawahara, S.; Kirino, Y.; Nagoshi, H.; Hirata, Y.; Nagano, T. Detection and Imaging of Nitric Oxide with Novel Fluorescent Indicators: Diaminofluoresceins. *Anal. Chem.* **1998**, *70*, 2446−2453.
(34) Goldstein, S.; Russo, A.; Samuni, A. Reactions of PTIO and Carboxy-PTIO with $\bullet\bullet NO_2$, and $O_2^{\bullet-}$. *J. Biol. Chem.* **2003**, *278*, 50949−50955.
(35) Hwang, C.; Sinskey, A. J.; Lodish, H. F. Oxidized redox state of glutathione in the endoplasmic reticulum. *Science* **1992**, *257*, 1496−1502.
(36) Jiang, X.; Chen, J.; Bajić, A.; Zhang, C.; Song, X.; Carroll, S. L.; Cai, Z.; Tang, M.; Xue, M.; Cheng, N.; et al. Quantitative real-time imaging of glutathione. *Nat. Commun.* **2017**, *8*, 16087.
(37) Liu, J.; Sun, Y.; Huo, Y.; Zhang, H.; Wang, L.; Zhang, P.; Song, D.; Shi, Y.; Guo, W. Simultaneous Fluorescence Sensing of Cys and GSH from Different Emission Channels. *J. Am. Chem. Soc.* **2014**, *136*, 574−577.
(38) Okazaki, S.; Takeshita, K. Irradiation of Phenolic Compounds with Ultraviolet Light Causes Release of Hydrated Electrons. *Appl. Magn. Reson.* **2018**, *49*, 881−892.
(39) Bakulin, A. A.; Rao, A.; Pavelyev, V. G.; van Loosdrecht, P. H. M.; Pshenichnikov, M. S.; Niedzialek, D.; Cornil, J.; Beljonne, D.; Friend, R. H. The Role of Driving Energy and Delocalized States for Charge Separation in Organic Semiconductors. *Science* **2012**, *335*, 1340−1344.

https://dx.doi.org/10.1021/jacs.0c10517
J. Am. Chem. Soc. 2021, 143, 868−878

(40) Ou, H.; Chen, X.; Lin, L.; Fang, Y.; Wang, X. Biomimetic Donor−Acceptor Motifs in Conjugated Polymers for Promoting Exciton Splitting and Charge Separation. *Angew. Chem., Int. Ed.* **2018**, *57*, 8729−8733.
(41) Wang, Y.; Zhao, D.; Ji, H.; Liu, G.; Chen, C.; Ma, W.; Zhu, H.; Zhao, J. Sonochemical Hydrogen Production Efficiently Catalyzed by Au/TiO2. *J. Phys. Chem. C* **2010**, *114*, 17728−17733.
(42) Chauvin, J.; Judee, F.; Yousfi, M.; Vicendo, P.; Merbahi, N. Analysis of reactive oxygen and nitrogen species generated in three liquid media by low temperature helium plasma jet. *Sci. Rep.* **2017**, *7*, 4562.
(43) Capaldo, L.; Ravelli, D. Hydrogen Atom Transfer (HAT): A Versatile Strategy for Substrate Activation in Photocatalyzed Organic Synthesis. *Eur. J. Org. Chem.* **2017**, *2017*, 2056−2071.
(44) Zhao, L.-M.; Meng, Q.-Y.; Fan, X.-B.; Ye, C.; Li, X.-B.; Chen, B.; Ramamurthy, V.; Tung, C.-H.; Wu, L.-Z. Photocatalysis with Quantum Dots and Visible Light: Selective and Efficient Oxidation of Alcohols to Carbonyl Compounds through a Radical Relay Process in Water. *Angew. Chem., Int. Ed.* **2017**, *56*, 3020−3024.
(45) Kobayashi, K. Pulse Radiolysis Studies for Mechanism in Biochemical Redox Reactions. *Chem. Rev.* **2019**, *119*, 4413−4462.
(46) Maroz, A.; Anderson, R. F.; Smith, R. A. J.; Murphy, M. P. Reactivity of ubiquinone and ubiquinol with superoxide and the hydroperoxyl radical: implications for in vivo antioxidant activity. *Free Radical Biol. Med.* **2009**, *46*, 105−109.
(47) Tanielian, C.; Wolff, C.; Esch, M. Singlet Oxygen Production in Water: Aggregation and Charge-Transfer Effects. *J. Phys. Chem.* **1996**, *100*, 6555−6560.
(48) Xie, X.; Tang, F.; Liu, G.; Li, Y.; Su, X.; Jiao, X.; Wang, X.; Tang, B. Mitochondrial Peroxynitrite Mediation of Anthracycline-Induced Cardiotoxicity as Visualized by a Two-Photon Near-Infrared Fluorescent Probe. *Anal. Chem.* **2018**, *90*, 11629−11635.
(49) Arteel, G. E.; Briviba, K.; Sies, H. Protection against peroxynitrite. *FEBS Lett.* **1999**, *445*, 226−230.
(50) Zhao, H.; Yin, R.; Wang, Y.; Lee, Y.; Luo, T.; Zhang, J.; Qiu, H.; Ambrose, S.; Wang, L.; Ren, J.; Yao, J.; Chen, D.; Wang, Y.; Liang, Z.; Zhen, J.; Wu, S.; Ye, Z.; Zeng, J.; Huang, N.; Gu, Y. Modulating mitochondrial morphology enhances antitumor effect of 5-ALAmediated photodynamic therapy both in vitro and in vivo. *J. Photochem. Photobiol., B* **2017**, *176*, 81−91.
(51) Zhao, Z.; Chan, P.; Li, H.; Wong, K.; Wong, R. N. S.; Mak, N.; Zhang, J.; Tam, H.; Wong, W.; Kwong, S. W.; Wong, W. Highly Selective Mitochondria-Targeting Amphiphilic Silicon(IV) Phthalocyanines with Axially Ligated Rhodamine B for Photodynamic Therapy. *Inorg. Chem.* **2012**, *51*, 812−821.
(52) Hatz, S.; Lambert, J. D. C.; Ogilby, P. R. Measuring the lifetime of singlet oxygen in a single cell: addressing the issue of cell viability. *Photochem. Photobiol. Sci.* **2007**, *6*, 1106−1116.
(53) Salmeron, M. L.; Quintana-Aguiar, J.; De La Rosa, J. V.; Lopez-Blanco, F.; Castrillo, A.; Gallardo, G.; Tabraue, C. Phenalenone-photodynamic therapy induces apoptosis on human tumor cells mediated by caspase-8 and p38-MAPK activation. *Mol. Carcinog.* **2018**, *57*, 1525−1539.
(54) Norman, K. G.; Canter, J. A.; Shi, M.; Milne, G. L.; Morrow, J. D.; Sligh, J. E. Cyclosporine A suppresses keratinocyte cell death through MPTP inhibition in a model for skin cancer in organ transplant recipients. *Mitochondrion* **2010**, *10*, 94−101.
(55) Galluzzi, L.; Larochette, N.; Zamzami, N.; Kroemer, G. Mitochondria as therapeutic targets for cancer chemotherapy. *Oncogene* **2006**, *25*, 4812−4830.
(56) Buytaert, E.; Dewaele, M.; Agostinis, P. Molecular effectors of multiple cell death pathways initiated by photodynamic therapy. *Biochim. Biophys. Acta, Rev. Cancer* **2007**, *1776*, 86−107.
(57) Pérez-Torres, I.; Manzano-Pech, L.; Rubio-Ruíz, M. E.; Soto, M.; Guarner-Lans, E. V. Nitrosative Stress and Its Association with Cardiometabolic Disorders. *Molecules* **2020**, *25*, 2555.
(58) He, X.; Situ, B.; Gao, M.; Guan, S.; He, B.; Ge, X.; Li, S.; Tao, M.; Zou, H.; Tang, B.; Zheng, L. Stereotactic Photodynamic Therapy Using a Two-Photon AIE Photosensitizer. *Small* **2019**, *15*, 1905080.
(59) Makarov, N. S.; Drobizhev, M.; Rebane, A. O. Two-photon absorption standards in the 550−1600 nm excitation wavelength range. *Opt. Express* **2008**, *16*, 4029−4047.
(60) Wang, S.; Wu, W.; Manghnani, P.; Xu, S.; Wang, Y.; Goh, C. C.; Ng, L. G.; Liu, B. Polymerization-Enhanced Two-Photon Photosensitization for Precise Photodynamic Therapy. *ACS Nano* **2019**, *13*, 3095−3105.

https://dx.doi.org/10.1021/jacs.0c10517
J. Am. Chem. Soc. 2021, 143, 868−878